

Received May 24, 2020, accepted June 2, 2020, date of publication June 4, 2020, date of current version June 17, 2020.

Digital Object Identifier 10.1109/ACCESS.2020.3000186

# Multilayer Fractional-Order Machine Vision Classifier for Rapid Typical Lung Diseases Screening on Digital Chest X-Ray Images

JIAN-XING WU<sup>ID1</sup>, (Member, IEEE), PI-YUN CHEN<sup>ID1</sup>, CHIEN-MING LI<sup>2</sup>, YING-CHE KUO<sup>1</sup>, (Member, IEEE), NENG-SHENG PAI<sup>ID1</sup>, AND CHIA-HUNG LIN<sup>ID1,3</sup>

<sup>1</sup>Department of Electrical Engineering, National Chin-Yi University of Technology, Taichung City 41170, Taiwan

<sup>2</sup>Division of Infectious Diseases, Department of Medicine of Chi Mei Medical Center, Tainan 710, Taiwan

<sup>3</sup>Artificial Intelligence Application Research Center, National Chin-Yi University of Technology, Taichung City 41170, Taiwan

Corresponding authors: Neng-Sheng Pai (pai@ncut.edu.tw) and Chia-Hung Lin (eechl53@gmail.com)

This work was supported by the Ministry of Science and Technology, Taiwan, under Contract MOST 108-2221-E-167-005-MY2 and Contract MOST 108-2218-E-167-007-MY2.

**ABSTRACT** Lung diseases can result in acute breathing problems and prevent the human body from acquiring enough oxygen. These diseases, such as pneumonia (P), pleural effusion (Ef), lung cancer, pneumothorax (Pt), pulmonary fibrosis (F), infiltration (In) and emphysema (E), adversely affect airways, alveoli, blood vessels, pleura and other parts of the respiratory system. The death rates of P and lung cancer are higher than those of other typical lung diseases. In visualization examination, chest radiography, such as anterior-posterior or lateral image viewing, is a straightforward approach used by clinicians/radiologists to diagnose and locate possible lung abnormalities rapidly. However, a chest X-ray image of patients may show multiple abnormalities associated with coexisting conditions, such as P, E, F, Pt, atelectasis, lung cancer or surgical interventions, which further complicate diagnosis. In addition, poor-quality X-ray images and manual inspection have limitations in digital image-automated classification. Hence, this study intends to propose a multilayer machine vision classifier to automatically identify the possible class of lung diseases within a bounding region of interest (ROI) on a chest X-ray image. For digital image texture analysis, a two-dimensional (2D) fractional-order convolution (FOC) operation with a fractional-order parameter,  $v = 0.3 - 0.5$ , is used to enhance the symptomatic feature and remove unwanted noises. Then, maximum pooling is performed to reduce the dimensions of feature patterns and accelerate complex computations. A multilayer machine vision classifier with radial Bayesian network and gray relational analysis is used to screen subjects with typical lung diseases. Anterior-posterior chest X-ray images from the NIH chest X-ray database (NIH Clinical Center) are enrolled. For digital chest X-ray images, with  $K$ -fold cross-validation, the proposed multilayer machine vision classifier is applied to facilitate the diagnosis of typical lung diseases on specific bounding ROIs, as promising results with mean recall (%), mean precision (%), mean accuracy (%) and mean F1 score of 98.68%, 82.42%, 83.57% and 0.8981, respectively, for assessing the performance of proposed multilayer classifier for rapidly screening lung lesions on digital chest X-ray images.

**INDEX TERMS** Chest Radiography, Multilayer machine vision classifier, region of interest, fractional-order convolution, gray relational analysis,  $K$ -fold cross validation.

## I. INTRODUCTION

Lung diseases refer to several types of diseases or disorders, such as infections, pneumonia (P), tuberculosis, pulmonary edema and lung cancer, which severely affect pulmonary

The associate editor coordinating the review of this manuscript and approving it for publication was Shiping Wen<sup>ID</sup>.

functions in one or both sides of the lungs and can lead to breathing problems or acute respiratory failure. These diseases also adversely affect airways, alveoli, blood vessels, pleura, interstitium and other parts of the respiratory system. Lung diseases have several types, and some of them are caused by bacterial, viral or fungal infections [1]. Other lung diseases are caused by environmental factors, such as

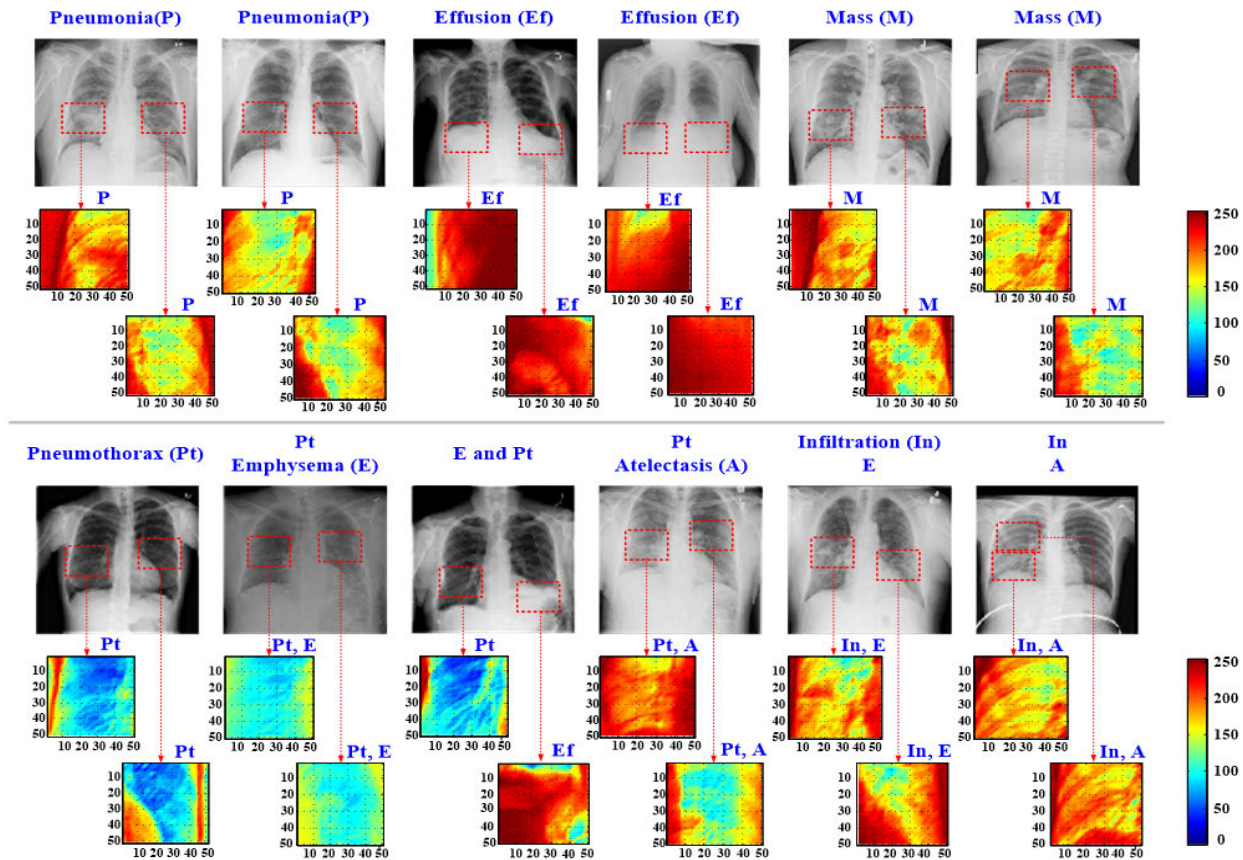


**FIGURE 1.** Typical lung diseases, including pneumonia (P), pleural effusion (Ef), mass (M), pneumothorax (Pt), inflammation (In), emphysema (E), and atelectasis (A).

asthma and lung cancer. In chronic lower respiratory diseases, including chronic obstructive pulmonary disease (COPD), emphysema (E) and chronic bronchitis, airways are narrowed, thereby reducing air flow. Spontaneous pneumothorax (Pt) may occur in approximately 70% of COPD cases [2], [3]. P is a lung infection disease that causes inflammation in the alveoli; consequently, fluid or pus fills the alveoli, and their ability to hold air is reduced. The death rate of pneumonia is higher in males than in females, i.e., about 68 deaths per 100,000 population in Taiwan. The risk of having these diseases in individuals older than 65 years or younger than 2 years is high. Pulmonary infiltration (In) is associated with P, tuberculosis and nocardiosis; in In, abnormal substances, such as pus, blood or dead cells, accumulate or spread through the interstices of the lung [4]. Smoking and environmental factors are high risk factors of lung cancer [5]. Although approximately 25% of lung cancers are not attributable to smoking, the incidence of lung cancer in nonsmokers has also increased, and more than 50% of cases occur in non-smoking females [6], [7]. The common causes of pleural effusion (Ef) are heart failure, P, pulmonary hypertension, pleuropulmonary malignancy and chest surgery; excessive amounts of fluid can also affect breathing, which can be divided into three Ef sizes: small (<500 mL), moderate (500 –1,000 mL) and large (>1,000 mL) effusion [8]–[11].

These lung diseases can be detected using imaged examinations with chest ultrasound, chest computed tomography (CT) scan and upright chest X-ray techniques [10], [12]–[15]. In visualization examination, a chest X-ray is an upright manner of bilateral lung imaging in the anterior-posterior or lateral view; digital image processing and artificial intelligence (AI) methods can be applied to rapidly detect lesions in chest X-ray images. Therefore, a complex lung disease classification can be accomplished for the automated screening of typical lung diseases, including P, Ef, M, Pt, In, E, and atelectasis (A), as seen in Figure 1.

When a lung disease gradually forms, the lung becomes inflamed and stiff, preventing the alveoli from fully expanding. This condition limits oxygen exchange to the bloodstream and carbon dioxide removal from the human body. As this disease progresses, the interstitium and walls of the alveoli thicken and impair pulmonary functions. Clinical diagnosis is based on the shortness of breath, cough, irregular fever, and wheezing to preliminarily screen lung conditions. Blood tests, pulmonary function tests, pulse oximetry, chest X-ray, chest CT, and biopsy/surgical biopsy examination may help accurately diagnose pulmonary conditions and track the underlying cause of a disease for medication or surgery. Although patients suffer from breathing problems or acute respiratory failure, their condition exacerbates to

hypoxia and hypercapnia, possibly affecting the heart and causing myocardial damage. Noninvasive electrocardiogram signals can reflect the myocardium condition in patients with P [16]. Blood tests are conducted to measure oxygen and carbon dioxide levels, which can be used to identify COPD. However, noninvasive measurements are easily influenced by instruments, humans, and environmental factors, such as baseline drift (respiration and myocardial excitation: lower frequency of  $<1$  Hz), electromyography interference (wide frequency ranges: 10 Hz–3 kHz), and power-line frequency interference (fixed frequency at 50 or 60 Hz) [16], [17]. Routine chest X-ray radiography is a first-line screening method with low-dose X-rays to view the chest cavity, which includes the lungs, heart, and chest wall. Upright digital imaging is a rapid and convenient method used to observe various lung conditions.

Any possible disease may appear as white portions in the chest cavity, and air spaces appear as black portions. Digital chest X-ray images can be used to directly identify and locate the class of abnormality through anterior-posterior or lateral views. However, pattern recognition with manual inspection has some limitations in practical applications: (1) poor-quality X-ray images should be enhanced in terms of the contents of the chest cavity; (2) diagnostic results depend on clinicians'/radiologists' interpretations and experiences; and (3) long inspection time is required to solve multimarker image classification problems. Therefore, in this study, an automatic computer-aided method based on a machine vision classifier is proposed to screen the bounding (ROI for identifying typical lung diseases (Figure 1). For specific feature extraction, feature detection, and image classification applications, a 2D first-order ( $v = 1.0$ ), fractional-order ( $0.0 < v < 1.0$ ), or second-order ( $v = 2.0$ ) convolution operation [10], [18]–[20] is applied to enhance images or detect edges within a bounding ROI. These 2D convolution operations are used to detect sharp changes in image brightness, such as discontinuities in depth and surface orientation or changes in material properties and illumination [21].

For digital image enhancement, integral differential convolution operators, such as Sobel, Prewitt and Laplacian Gaussian operators, do well in high-frequency contour features in an image. However, their performance significantly deteriorates when they are applied to smoothing regions. Conversely, a fractional-order operator has the capability to preserve high-frequency contour features and improve low-frequency texture details in a smoothing region. This spatial domain-based method involving a fractional-order operator can also be used to avoid noise introduction while enhancing image [22], [23]. The FOC process is able to enhance the edge information in the region where the gray gradient changes in high frequency variants and also retains the low-frequency contour information of the low-quality X-ray images. Hence, spatial domain-based convolution can be used to enhance the possible lesion and remove noise for further machine-vision automatic inspection. Hence, 2D FOC in horizontal and vertical directions is applied

to image enhancement. For automated pattern recognition, including image enhancement with a 2D convolution operation, pooling process, flattening process and pattern recognition, a spatial domain-based convolution operation is combined with a multilayer machine vision classifier to deal with digital chest X-ray images [1], [24]–[27]. The structure of this combination is shown in Figure 2(a). A multilayer fully connecting network with a radial Bayesian network (RBN) [26], [27] and gray relational analysis (GRA) as an adaptive algorithm [28]–[32] is employed to rapidly screen typical lung diseases. In experimental validations, anterior-posterior chest X-ray images from the National Institutes of Health (NIH) chest X-ray database (NIH Clinical Center) are enrolled [33]. For digital X-ray images (with labeled classes), the proposed multilayer machine vision classifier is demonstrated with K-fold cross-validation to facilitate the diagnosis of lung diseases on bounding ROIs and further explore clinical treatments.

The remainder of this article is organized as follows. Section II describes the methodology, including 2D fractional-order convolution, development of multilayer fractional-order machine vision classifier, experimental setup and flowchart of a rapid screening procedure for lung diseases. Section III provides the experimental results, discussion and comparison with traditional multilayer neural networks. Section IV presents the conclusion.

## II. METHODOLOGY

### A. EXPERIMENTAL SETUP

The NIH Clinical Center has released privacy chest X-ray images (more than 30,000 patients) and their corresponding data for scientific research [33]. Through clinical research, clinician-investigators can translate research results and experiences into better therapies, treatments, and interventions in clinical trials. Scientific researchers can also analyze and appraise datasets and design a computer-aided tool for automatically detecting lung diseases by using images with labeled classes [33], [34]; for example, training artificial intelligence (AI) methods can help clinicians make better diagnostic decisions.

AI-based and AI-aided methods have some abilities [35]:

- rapid screening of possible abnormalities on a bounding ROI for a large amount of digital images,
- electronic enhancement (magnification and optimization) of the parts of the target ROI,
- identification of slow changes in possibly occurring abnormalities on the bounding ROI,
- quick location and extraction of specific features to support real time applications

With an ongoing clinical investigation on the addition of a large dataset, AI-based and AI-aided methods can gradually refine diagnostic precision in clinical applications. Figure 3 shows a flowchart of a rapid screening procedure of typical lung diseases and a pathway of continuous learning in ongoing clinical evaluation, including image collection, image biomarker, image enhancement, trained

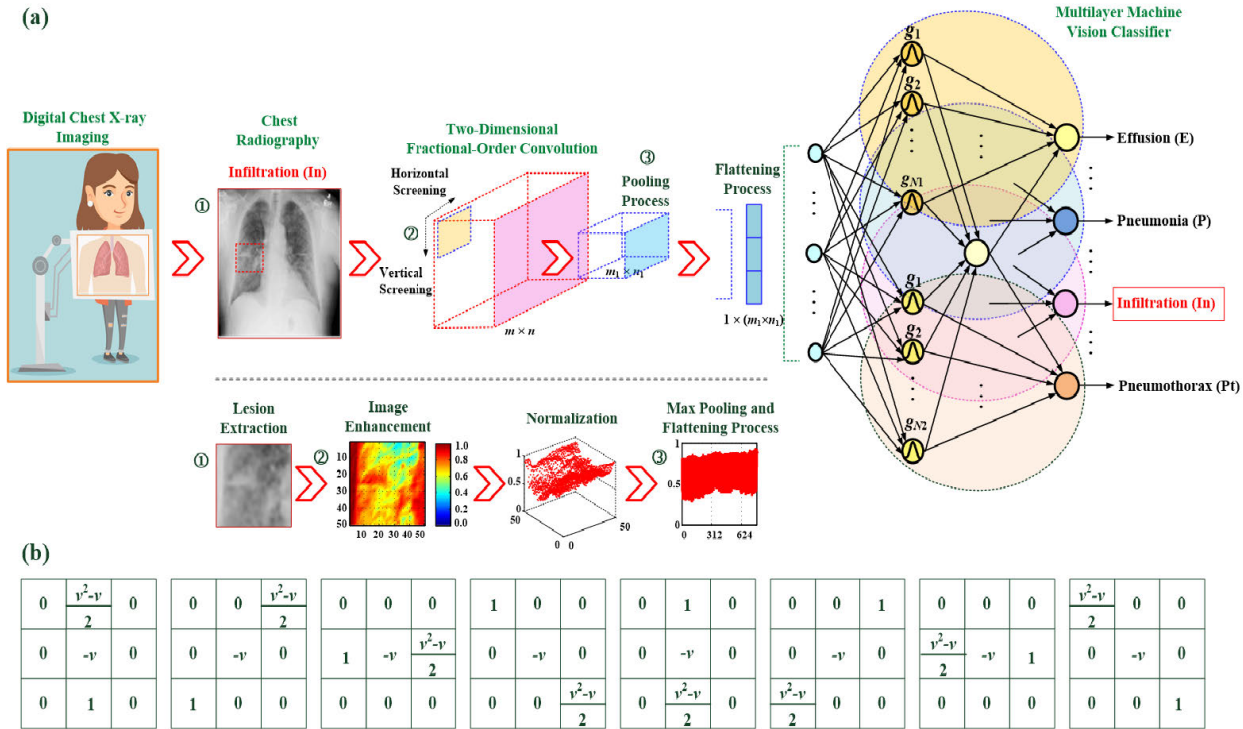


**FIGURE 2. Multilayer fractional-order machine vision classifier for the rapid screening of typical lung diseases. (a) Structure of the multilayer fractional-order machine vision classifier; (b) eight combinations of fractional-order convolution operators to perform digital image enhancement, including negative x-coordinate, right upward diagonal, positive y-coordinate, right downward diagonal, positive x-coordinate, left downward diagonal, negative y-coordinate and left upward diagonal.**

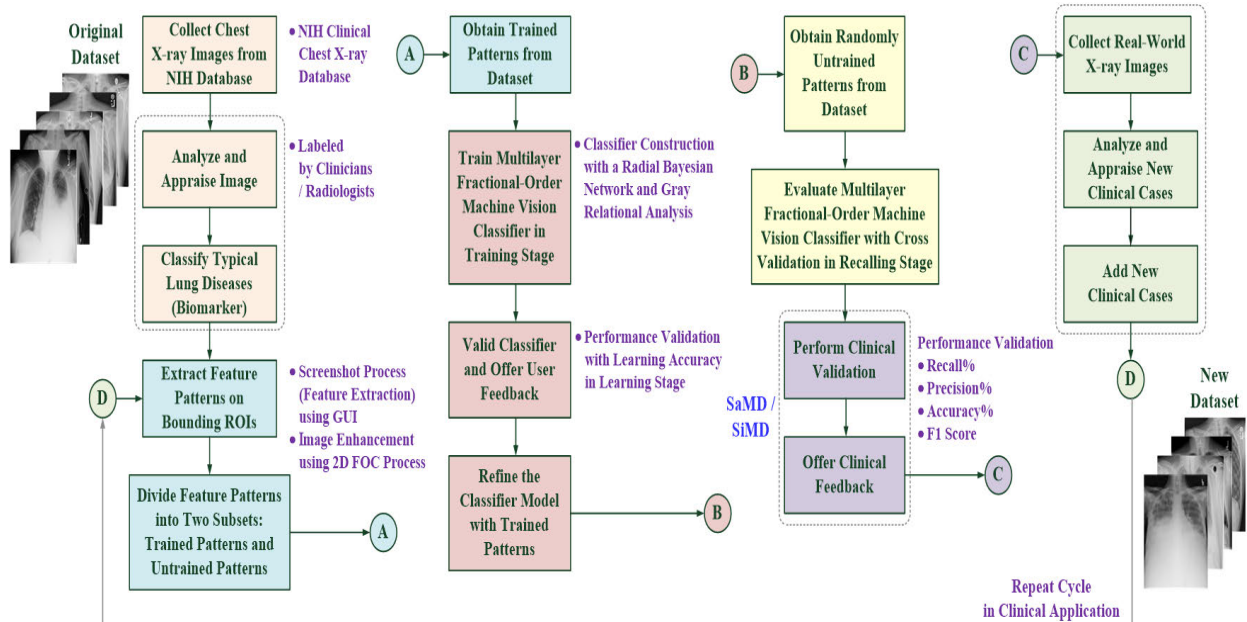


**FIGURE 3. Flowchart for a rapid typical lung disease screening procedure and related tools and methods in training stage, recalling stage, performance validation and clinical application.**

and untrained dataset establishment, classifier training and testing in training and recalling and performance validation with recall (%), precision (%), accuracy (%) and F1 score indices. A total of 230 subjects aged 1–89 years are selected

for the experimental analysis; they include 100 females (mean age:  $44.40 \pm 14.06$  years) and 130 males (mean age:  $48.00 \pm 17.56$  years), as shown in Table 1 [33]. Chest X-ray images are collected from the 230 subjects and

**TABLE 1.** The profile of the enrolled subjects [33].

Aged Range	Female (F)	Male (M)
0 – 30 (41)	22.63 ± 7.17 (19)	20.50 ± 6.31 (22)
30 – 60 (144)	46.22 ± 12.52 (69)	46.17 ± 13.33 (75)
60 – 90 (45)	65.83 ± 12.57 (12)	70.52 ± 13.41 (33)
0 – 90 (230)	44.40 ± 14.06 (100)	48.00 ± 17.56 (130)

converted into a tagged image file (TIF) format. Each image is digitized to a resolution of  $96 \times 96$  dots per inch, thereby producing 24 bits per pixel that is then incorporated into a  $190 \times 230$  pixel image (43,700 pixels). Feature patterns on bounding ROIs are required to enhance contents and remove unwanted noise via spatial domain-based convolution. For clinical applications in medical devices or commercial off-the-shelf (COTS) platforms and virtual networks, such as software as a medical device (SaMD) or software in a medical device (SiMD) [36], [37], the proposed machine vision classifier with a meta-learning refining scheme can be used to continuously collect real-world trained datasets relying on end users and clinical feedback. A continuous learning-based algorithm is introduced to keep learning automatically with real-world information (consultation with clinicians/radiologists), leading to changes in the intended use.

### B. SPATIAL DOMAIN-BASED CONVOLUTION OPERATION

Fractional-order multi-scale operators are designed for fractional differential and fractional integral operations, such as Grünwald–Letnikov (G–L) and Riemann–Liouville (R–L) definition [18], [23], which are applied to texture enhancement in pattern recognition, image restoration, medical image processing and so on. Although image resolution is low, texture enhancement needs to adequately act in real time. An operator structure includes single direction, multi-direction and non-regular region. However, a single direction operator has a poor performance in capturing an image gradient. Spatial domain-based operators have multiple directions and an anti-rotation capability to obtain multiple directions' features; for example, Figure 2(b) shows eight direction operators, which include the directions of negative x- coordinate, right upward diagonal, positive y-coordinate, right downward diagonal, positive x-coordinate, left downward diagonal, negative y-coordinate and left upward diagonal [18], [20], [38], [39]. Fractional-order operators can be rotated clockwise every  $45^\circ$  (rotation invariant) in eight directions. In this study, a multi-scale operator is designed with a G–L fractional-order differentiator, and can be expressed as general form [18]:

$$\frac{d^v s(t)}{dt^v} \cong \frac{t^{-v} n^v}{\Gamma(-v)} \sum_{k=0}^{n-1} \frac{\Gamma(k-v)}{\Gamma(k+1)} s(t - \frac{kt}{n}) \quad (1)$$

where  $s(t)$  is the time-varying signal in a one-dimensional (1D) signal;  $v$  is the fractional-order parameter,  $0 < v < 1$ ,  $v \in R$ ; and  $\Gamma(\bullet)$  is the Gamma function. For a 2D digital image processing, Equation (1) can be modified and proximately expressed in horizontal ( $x$ ) and vertical ( $y$ ) directions as follows:

$$\begin{aligned} \frac{d^v I(x, y)}{dx^v} &\cong a_0 I(x, y) + a_1 I(x-1, y) + a_2 I(x-2, y) \\ &\quad + a_3 I(x-3, y) + \cdots + a_{n-1} I(x-n+1, y) \end{aligned} \quad (2)$$

$$\begin{aligned} \frac{d^v I(x, y)}{dy^v} &\cong a_0 I(x, y) + a_1 I(x, y-1) + a_2 I(x, y-2) \\ &\quad + a_3 I(x, y-3) + \cdots + a_{n-1} I(x, y-n+1) \end{aligned} \quad (3)$$

where  $I(x, y)$  is the pixel value at location  $(x, y)$  in an X-ray image,  $I, I(x, y) \in [0, 255]$ ;  $x = 1, 2, 3, \dots, p$  and  $y = 1, 2, 3, \dots, q$ ,  $p$  and  $q$  are the image width and height, respectively; and coefficients,  $a_0, a_1, a_2, a_3, \dots$ , and  $a_n$ , are expressed below [18]:

$$\begin{aligned} a_0 &= 1, a_1 = (-v), a_2 = \frac{(-v)(-v+1)}{2}, \\ a_3 &= \frac{(-v)(-v+1)(-v+2)}{2}, \dots, a_k = \frac{\Gamma(k-v)}{(k)!\Gamma(-v)}, \quad \text{and} \\ \dots, a_{n-1} &= \frac{\Gamma(n-v-1)}{(n-1)!\Gamma(-v)} \end{aligned}$$

As  $k$  approaches  $n$  ( $k \rightarrow n$ ), where  $n = 2m - 2$ , a  $(2m-1) \times (2m-1)$  fractional-order mask can be designed;  $n$  should be an even number ( $n = 2, 4, 6, \dots$ ) to ensure that the fractional-order mask has a specific center. Hence,  $3 \times 3$ ,  $5 \times 5$ , ..., and  $(2m-1) \times (2m-1)$  fractional -order masks ( $m = 2, 3, 4, \dots$ ) can be implemented for discrete pixel processing. In this study, the size of  $m = 2$  is selected to construct  $3 \times 3$  mask matrices, as seen in Figure 2(b). A spatial domain-based convolution operation can be implemented on the negative  $x$ -coordinate and the negative  $y$ -coordinate with three coefficients, namely,  $a_0, a_1$  and  $a_2$ , which are the first three terms in Equations (2) and (3). In the 2D digital image, the fractional-order gradient can be defined as

$$\nabla^v I(x, y) = \begin{bmatrix} G_x^v I \\ G_y^v I \end{bmatrix} = \begin{bmatrix} \frac{\partial^v I(x, y)}{\partial x^v} & \frac{\partial^v I(x, y)}{\partial y^v} \end{bmatrix}^T \quad (4)$$

$$|\nabla^v I(x, y)| = \sqrt{(G_x^v I)^2 + (G_y^v I)^2} \cong |G_x^v I| + |G_y^v I| \quad (5)$$

Equation (5) is a simplified form, which can speed up computations for 2D convolution operation. It can also be normalized as

$$\nabla I = \frac{|G_x^v I| + |G_y^v I|}{255} \quad (6)$$

With the use of the operators  $G_x^v I(x, y)$  and  $G_y^v I(x, y)$ , the spatial domain-based FOC operations in a 2D space are

used to enhance the X-ray image by convolving both horizontal and vertical directions and can be expressed as

$$G_x^v I(x, y) = \sum_{i=-\frac{h-1}{2}}^{\frac{h-1}{2}} \sum_{j=-\frac{h-1}{2}}^{\frac{h-1}{2}} M_x(i, j) I(x + i, y + j) \quad (7)$$

$$G_y^v I(x, y) = \sum_{j=-\frac{h-1}{2}}^{\frac{h-1}{2}} \sum_{i=-\frac{h-1}{2}}^{\frac{h-1}{2}} M_y(j, i) I(x + j, y + i) \quad (8)$$

where  $h = 3$  is the size of the mask matrix for the  $3 \times 3$  fractional-order mask, and  $M_x(i, j) = M_y(j, i)$  is the element in the fractional-order mask:

$$M_x = \begin{bmatrix} 0 & \frac{v^2 - v}{2} & 0 \\ 0 & -v & 0 \\ 0 & 1 & 0 \end{bmatrix},$$

$$M_y = M_x^T = \begin{bmatrix} 0 & 0 & 0 \\ \frac{v^2 - v}{2} & -v & 1 \\ 0 & 0 & 0 \end{bmatrix} \quad (9)$$

where  $i$  and  $j$  are the rows and column number in the mask matrix, respectively. In mask matrices,  $M_x$  and  $M_y$ , as shown in Equation (9), the summation of all elements is a nonzero value. Each convolution computation involves row and column elements, and each element is multiplied by the corresponding input discrete pixel values, which are used to enhance X-ray images via convolution with the structure tensor masks  $M_x$  and  $M_y$ ;  $\nabla I$  is the normalized gray gradient,  $\nabla I \in [0, 2]$ .

### C. FEATURE (LESION) EXTRACTION AND CLASSIFIER DESIGN

A machine vision classifier has the capability to screen typical lung diseases, so X-ray image datasets should be established first to train a classifier model. Chest X-ray images are obtained from the NIH chest X-ray database [33] to obtain the datasets. Feature patterns within ROIs with a fixed size are extracted to enhance the classification performance, and feature patterns are enhanced via the following 2D fractional-order convolution process:

- In feature pattern extraction, locations and specific boundaries on ROIs from the chest X-ray images are selected by clinicians/radiologists. A fixed bounding box (B-box) with  $50 \times 50$  pixels (2,500 elements) is designed to capture the lesion features involving the possible lesion region, which is denoted by “①” in Figure 2(a). The B-box can be used to feed the fixed feature patterns into the input layer of the machine vision classifier.
- In feature enhancement, the 2D discretized convolution operation is performed on  $I$  with  $M_x$  and  $M_y$ , and the lesion in the specific B-box is selected via the screenshot process, as indicated by “②” in Figure 2(a). The feature pattern is normalized using Equations (5) to (8).

Figure 4 shows some 2D and 3D feature patterns of image enhancement for typical lung diseases, including Pt, Ef, P, In, F, F and In, M, M and F, and Pt and E in the right lung (RL) or the left lung (LL). Each feature pattern is obtained from the convolutional layer, its dimension is reduced from  $50 \times 50$  pixels to  $25 \times 25$  pixels (625 elements), and memory requirement is decreased via maximum pooling and flattening processing [1], [24], [25], as denoted by “③” in Figure 2(a).

- In screenshot processing, the LabWindows™/CVI™ 2019 application software (NI™, Austin, TX, USA) is used to obtain a screenshot graphical user interface (GUI).

Its framework can be used to choose the feature pattern as an input pattern via a movable fixed B-box, which gives a feature pattern to be displayed on a computer screen that presents the screening results, as seen in Figure 5.

In clinical applications, clinicians or radiologists can move the fixed B-box by sliding it to select the possible lesion within the chest cavity. After the image is enhanced, a  $2 \times 2$  max mask is used as a sliding filter to choose the maximum value of the component of feature patterns.

Then, a given feature pattern is flattened from a matrix form to a vector form, which is fed into a classifier to perform the pattern recognition tasks. In this study, a combining RBN and GRA computational network is carried out in a GRA-based fully connecting multilayer classifier for screening typical lung diseases. In the GRA method, the numerical measure of similarity between two data streams is used to define the reference sequence (testing pattern),  $\Phi_0 = [\nabla I_1(0), \nabla I_2(0), \nabla I_3(0), \dots, \nabla I_i(0), \dots, \nabla I_{n'}(0)]$ ,  $i = 1, 2, 3, \dots, n'$  ( $n' = 625$  in this study), and  $K$  comparative sequences (training pattern),  $\Phi_k = [\nabla I_1(k), \nabla I_2(k), \nabla I_3(k), \dots, \nabla I_{n'}(k)]$ ,  $k = 1, 2, 3, \dots, K$ . The output of GRA as the gray grade (GG) is distributed between 0 and 1 as a Gaussian function and can be defined as follows [28], [40]:

Gray grade :  $g(k)$

$$= \xi \exp\left(-\frac{1}{2}\left(\frac{\sqrt{\sum_{i=1}^{n'} (\Delta d_i(k))^2}}{\sigma}\right)^2\right) \quad (10)$$

Euclidean distance (ED) :  $\Delta d_i(k)$

$$= \nabla I_i(0) - \nabla I_i(k) \quad (11)$$

$ED(k)$

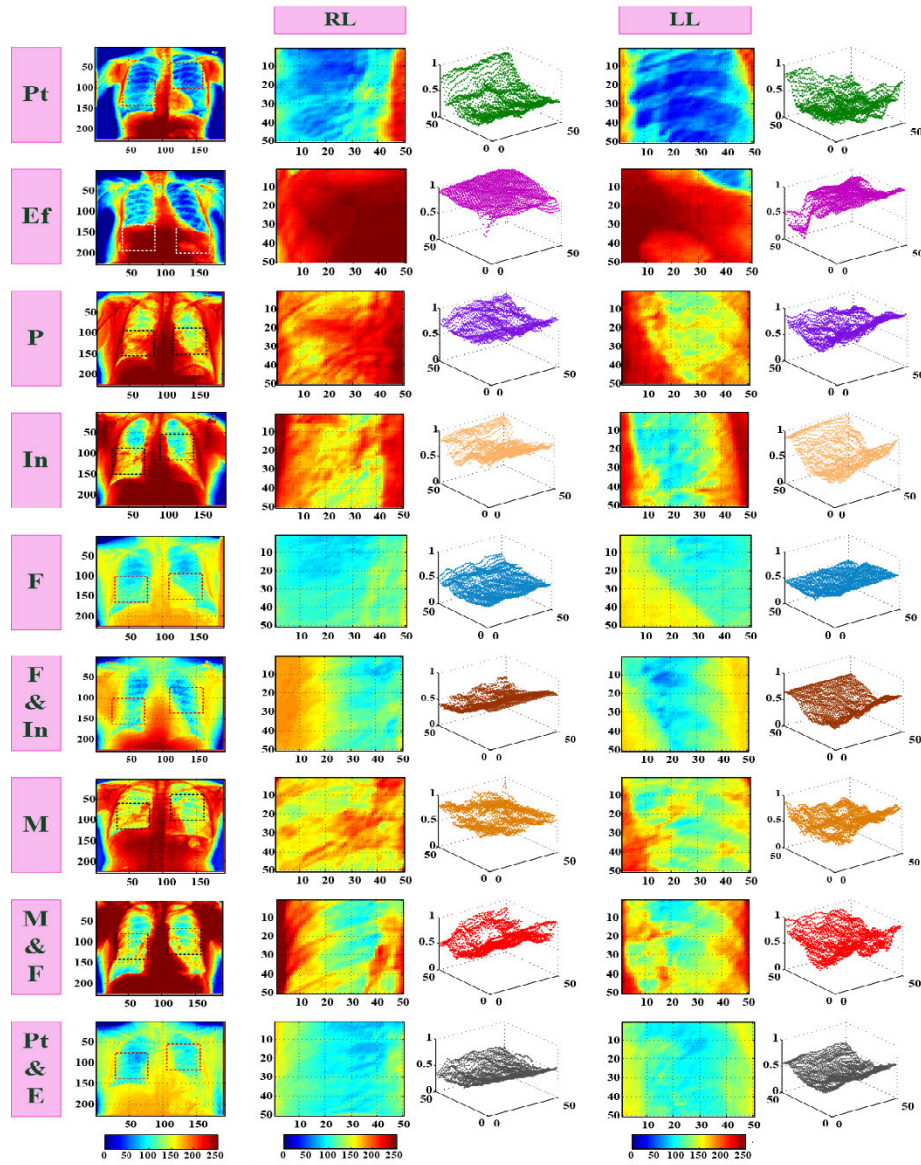
$$= \sqrt{\sum_{i=1}^{n'} (\Delta d_i(k))^2} \quad (12)$$

Variance :  $\sigma^2$

$$= (\Delta d_{\max} - \Delta d_{\min})^2 \quad (13)$$

$\Delta d_{\max}$

$$= \max_{\forall k} [\max_{\forall i} \Delta d_i(k)], \Delta d_{\min} = \min_{\forall k} [\min_{\forall i} \Delta d_i(k)] \quad (14)$$



Note: Pt-Pneumothorax; Ef-Effusion; P-Pneumonia; In-Infiltration; F-Fibrosis; M-Mass; E-Emphysema

**FIGURE 4.** Preliminary results of image enhancement in 2D and 3D feature patterns of ROIs for typical lung diseases, including Pt, Ef, P, In, F, F & In, M, M & F, and Pt & E.

where  $\xi$  is the recognition coefficient (RC),  $\xi \in (0, 5]$ , which is used to make the GG grade more distinguishable between a pattern ( $\Phi_0$ ) and  $k$ th patterns ( $\Phi_k$ ), as seen in GGs versus EDs in Figure 6(a).  $K$  comparative sequences ( $\Phi_k$ ,  $k = 1, 2, 3, \dots, K$ ) are established by the training patterns for seven typical lung diseases (Pt, Ef, E, In, M, P, and F) and the normal (N) condition, as shown in Figure 6(b); these sequences can be represented as

$$\Phi = \begin{bmatrix} \Phi_1 \\ \Phi_2 \\ \vdots \\ \Phi_k \\ \vdots \\ \Phi_K \end{bmatrix} = \begin{bmatrix} \nabla I_1(1) & \nabla I_2(1) & \cdots & \nabla I_{n'}(1) \\ \nabla I_1(2) & \nabla I_2(2) & \cdots & \nabla I_{n'}(2) \\ \vdots & \ddots & \cdots & \vdots \\ \nabla I_1(k) & \nabla I_2(k) & \cdots & \nabla I_{n'}(k) \\ \vdots & \ddots & \cdots & \vdots \\ \nabla I_1(K) & \nabla I_2(K) & \cdots & \nabla I_{n'}(K) \end{bmatrix} \quad (15)$$

The training patterns can be combined as  $\Phi = [\Phi_1, \Phi_2, \dots, \Phi_k, \dots, \Phi_K] = [\Phi_1, \dots, \Phi_{N1} | \Phi_1, \dots, \Phi_{N2} | \Phi_1, \dots, \Phi_{N3} | \dots | \Phi_1, \dots, \Phi_{N8}]$ ,  $N_j, j = 1, 2, 3, \dots, 8$ , is the number of training pattern for Class # $j$ , and  $K = N_1 + N_2 + N_3 + \dots + N_8$  (as seen in Figure 6(b));  $\Delta d_{max}$  and  $\Delta d_{min}$  are the maximum and minimum differences, respectively; standard deviation ( $\sigma$ ) is estimated by using  $(\Delta d_{max} - \Delta d_{min})$ . The GGs use the EDs to measure the similarity degree between a testing pattern and  $K$  training patterns. The  $g(k)$  of GG is inversely proportional to  $ED(k)$  as  $ED_{min} = \min(ED(k)) \leq ED(k) \leq ED_{max} = \max(ED(k))$ ,  $\forall k = 1, 2, 3, \dots, K$ ;  $ED(k) \rightarrow ED_{max}$ , then  $g(k) \rightarrow 0$ ; and  $ED(k) \rightarrow ED_{min}$ , then  $g(k) \rightarrow \xi$ . If  $ED_{min}$  and  $ED_{max}$  are very small, the RC is used to select  $\xi \gg 1$  to increase the contrast between  $\Phi_0$  and  $\Phi_k$ . Parameter,  $\xi = 5$ , is chosen in the present study [28], [40].

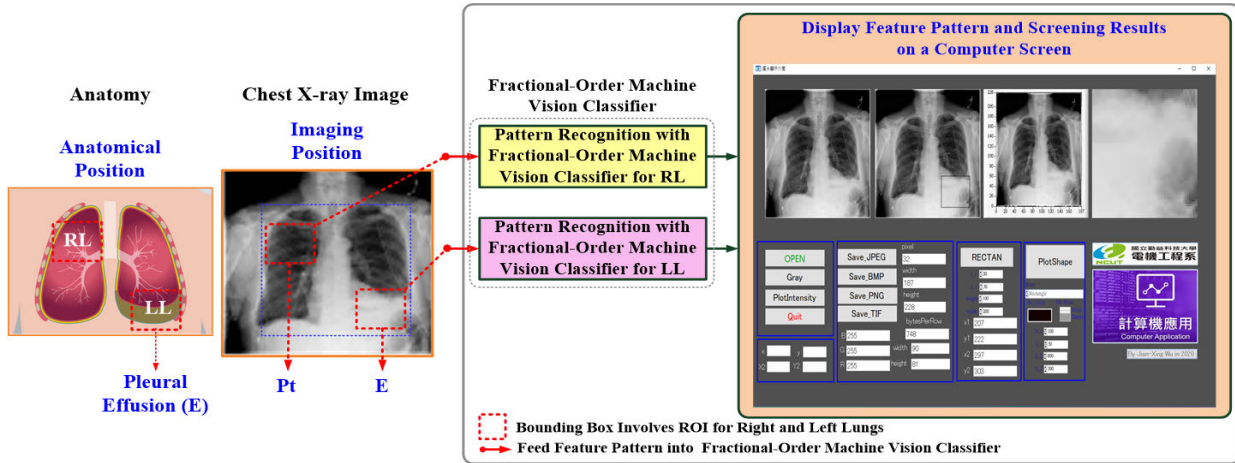


**FIGURE 5.** Screenshot processing and pattern recognition by using the graphical user interface and proposed multilayer machine vision classifier.

Then, as seen in Figure 2(a), the RBN represents the relationships of output GGs among the eight classes ( $m = 8$ ) for both right and left lungs, as follows:

$$y_j = \sum_{k=1}^K w_{kj} g(k) / \sum_{k=1}^K g(k) \quad (16)$$

$$w_{kj} = \begin{cases} 1, & k \in \text{Class } j \\ 0, & k \notin \text{Class } j \end{cases} \quad j = 1, 2, 3, \dots, 8 \quad (17)$$

where  $w_{kj} = y_j(k)$  is the weighting value,  $w_{kj} \in [0,1]$ ;  $K \times 8$  connecting weights are created between  $K$  GG functions,  $g(k)$ , and eight output nodes,  $y_j$ , by output training patterns, as seen in Figure 6(b), which are encoded as binary values with a value of “1” for possible class, and all other classes are encoded with a “0” value, for eight classes; an output (label) vector can be represented as  $\mathbf{Y} = (\text{Pt}, \text{Ef}, \text{E}, \text{In}, \text{M}, \text{P}, \text{F}, \text{N}) = (y_1, y_2, y_3, y_4, y_5, y_6, y_7, y_8)$ ,  $y_j \in [0, 1]$ . The final output value  $O_j$  is given by the following hard limit function:

$$O_j = \begin{cases} 1, & y_j \geq 0.5 \\ 0, & y_j < 0.5, \end{cases} \quad j = 1, 2, 3, \dots, 8 \quad (18)$$

where the threshold value 0.5 is set to confirm the decision boundary separating “disease present” from “disease absent,” and the final outputs  $O_j$ , where  $O_j \in [0, 1]$ , are binary values representing the possible class.

The proposed GRA-based classifier is affected by the width of the GG function (Gaussian function), as presented in Equation (10). As the width of the function decreases, decision boundaries can become increasingly nonlinear for nonlinear separable classification problems in chest X-ray images. The RBN with GG functions can be used to approximate the arbitrary function, i.e., self-adjusting manner by using Equations (13) and (14), for nonlinear mapping relationships between the input and output patterns without statistical estimation and iteration computations [28], [40]. In addition,  $RC$  can be tuned by clinicians/radiologists to

enhance the distinction between a testing pattern and training patterns. With the addition of the new input–output paired training patterns in comparative sequences, the deviation of a reference sequence and comparative sequences can be applied to automatically control the width of the GG function in this dynamic adjusting model and achieve clinically relevant computer-aided decision-making (CADM) in real-world applications.

### III. EXPERIMENTAL RESULTS AND DISCUSSION

A total of 230 subjects from the NIH chest X-ray database were enrolled in this study. The subjects were classified into two groups: (1) 100 subjects in the female group and (2) 130 subjects in the male group; their related data are presented in Table 1 [35]. A total of 414 feature patterns were captured from all the subjects: 68 Pts, 50 Efs, 30 Es, 56 Ins, 50 Ms, 60 Ps, 50 Fs, and 50 Ns. They were then divided into 207 trained datasets and 207 untrained datasets. Each dataset was a pair of a feature pattern (input) and a label pattern (biomarker), as shown in Figure 6(b). The first group of datasets was used to facilitate the machine vision classifier training. All feature patterns and labels were extracted and mined with a screenshot GUI from the frontal view of the X-ray images. Image labels, such as single label or multiple labels, were mined from radiologists. Each pattern was a  $50 \times 50$  pixel image (2,500 pixels). Hence, these feature patterns could be utilized to train and validate the proposed classifier. The proposed digital imaging process and screening algorithms were designed on a tablet PC by using a high-level programming language in LabVIEW (NI<sup>TM</sup>, Austin, TX, USA) and MATLAB 9.0 (MathWorks, Natick, MA, USA). The application program was used with a graphics processing unit (GPU) on a tablet PC (Intel® Xeon®, CPU E5-2620, v4, 2.1 GHz and 64 GB of RAM; GPU: NVIDIA Quadro P620, 64-bit Windows 10.0 operating system), which enables faster digital image processing and disease screening. The feasibility study of the proposed image enhancement

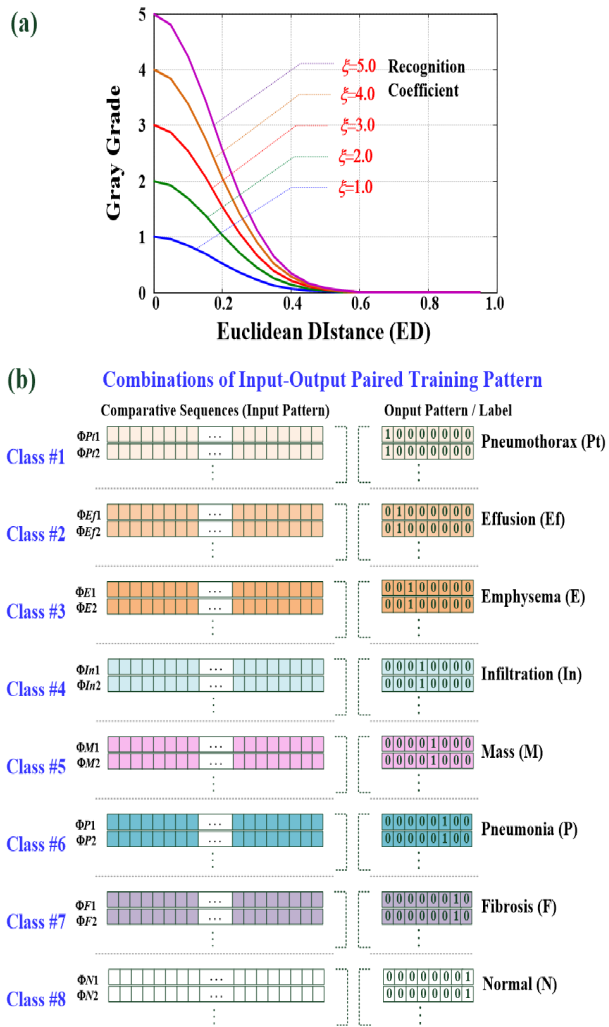


**FIGURE 6.** Gray grade function and input–output paired training patterns. (a) Gray grades versus Euclidean distances with recognition coefficients,  $\xi = 1.0\text{--}5.0$ , and (b) Input–output paired training patterns for a normal condition and seven typical lung diseases.

processing and screening methods were validated as described in detail in the following sections.

#### A. GRA-BASED CLASSIFIER TRAINING AND TESTING

In convolution processes, the fractional-order convolution operation in the horizontal and vertical directions was used to enhance the feature pattern within the ROI, as seen in the B-boxes in Figure 7. The fractional-order parameter ( $v$ ) was set from 0 to 1 and could not totally fit the X-ray image enhancement. The suggested appropriate parameters were  $v = (0.3, 0.5) = \{v|0.3 \leq v < 0.5\}$ , as seen in the local image enhancement for the possible focus in the right or left cavity; for example, with  $v = 0.3$ , the feature patterns of Pt and Ef are shown in Figure 7(a). The image processing results were similar and stable from  $v = 0.3$  to  $v = 0.4$ . Thus, the fractional-order mask with  $v = 0.3$  was assigned for all X-ray images in this study.

After the images were enhanced, the pooling process with a  $2 \times 2$  max filter was employed to reduce the dimensions of the input feature pattern from  $50 \times 50$  to  $25 \times 25$  in the pooling layer. Then, the pooled feature pattern was flattened in the matrix form to a vector form ( $1 \times 625$ ), as seen in the processing procedure in Figure 8. This pattern was then fed into the inputs of GRA-based classifier. A total of 207 trained patterns were randomly selected from different labeled classes to train the machine vision classifier at the learning stage, and the 207 remaining feature patterns were randomly chosen to evaluate the performance of the classifier with a K-fold cross-validation at the recalling stage. At the learning stage, after image convolution and pooling processes were conducted, 207 paired input–output training patterns could be selected to train the GRA-based classifier:  $\Phi_k = [\nabla I_1(k), \nabla I_2(k), \nabla I_3(k), \dots, \nabla I_{625}(k)]$  and  $[y_1(k), y_2(k), y_3(k), y_4(k), y_5(k), y_6(k), y_7(k), y_8(k)] = [0, 0, 0, 0, 0, 0, 1]$ ,  $k = 1, 2, 3, \dots, 207$ ,  $y_j(k) \in [0, 1]$ .

Hence, we could produce  $207 \times 625$  and  $207 \times 8$  connecting weighted values. Hence,  $207 \times 625$  and  $207 \times 8$  connecting weights could be produced in the GRA-based classifier. The output patterns were encoded as the binary values “1” or “0” for possible class identification and stored as weighting values by using Equation (17). For example, a weighting vector,  $[y_1(k), y_2(k), y_3(k), y_4(k), y_5(k), y_6(k), y_7(k), y_8(k)] = [0, 0, 0, 0, 0, 0, 1]$ , represented N because no pathology was found in any of the considered typical diseases. The 207 trained patterns contained 34 Pts, 25 Efs, 15 Es, 28 Ins, 25 Ms, 30 Ps, 25 Fs, and 25 Ns. The structure of the GRA-based classifier could be determined by identifying the number of training patterns ( $K = 207$ ) and the dimension of the input pattern ( $n' = 625$ ) and the output pattern ( $j = 1, 2, 3, \dots, 8$ ), which used the limited number of available training patterns on the learning task. Thus, a classifier consisting of 625 input nodes, 207 GG functions in RBN, and 8 output nodes was constructed. Parameter  $RC$  was  $\xi = 5$  in each GG function. The proposed GRA-based classifier employed a pattern recognition mechanism in a straightforward mathematical operation to process numerical computations for numerical and binary data analysis. Consequently, input–output paired patterns could be increased without adjusting any of the parameters at the learning stage.

For a case study, findings included multiple pathological symptoms as the right Pt and the small left Ef in digital image preprocessing. Image enhancement, pooling and flattening processes are shown in Figure 8(a). Two untrained patterns (olive line, mean gray gradient = 0.3340; red line patterns, mean gray gradient = 0.8497, respectively, as seen in Figure 8(a)) could be fed into the GRA-based classifier to identify the possible single or multiple classes. First, with the GG functions,  $EDs$  were employed to measure the similarity degree between 2 untrained patterns and 207 trained patterns. If the untrained pattern was similar to any trained pattern, the  $ED$  would have a minimum value (2.6700 for Pt and 1.5585 for Ef), and the GG would have a maximum value (1.3652 for Pt and 1.3526 for Ef) in RBN; for example,

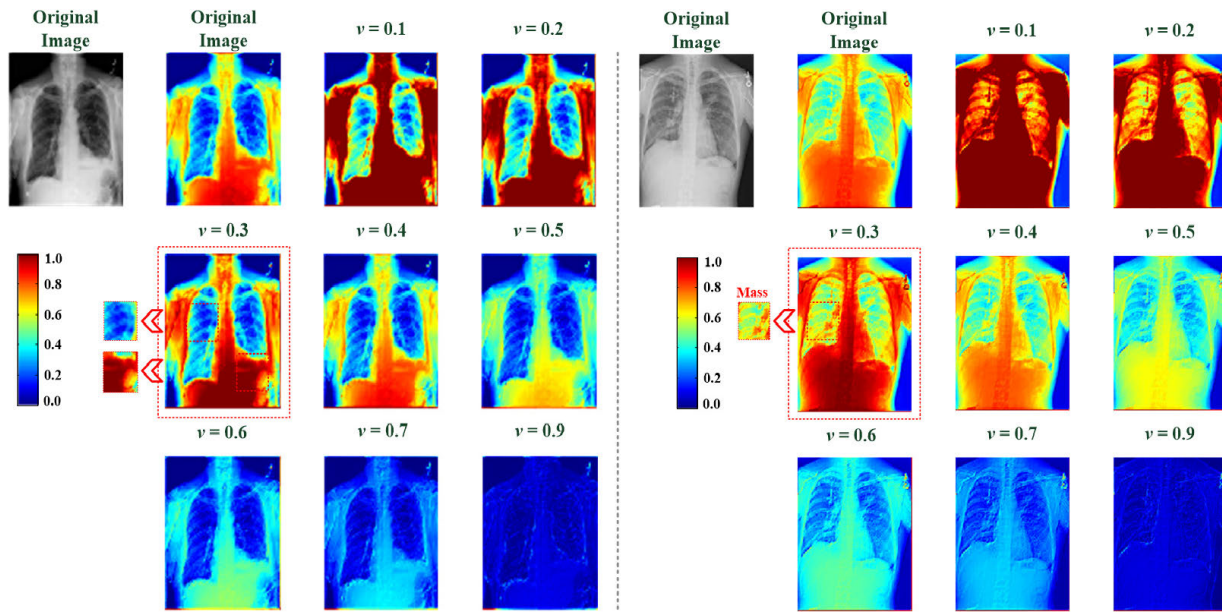


**FIGURE 7.** Image enhancement via 2D convolution with different fractional-order parameters,  $v = 0.10 – 0.90$ , for chest X-ray images. (a) Case study in subject with pneumothorax (Pt) and pleural effusion (Ef), (b) Case study in subject with mass (M).

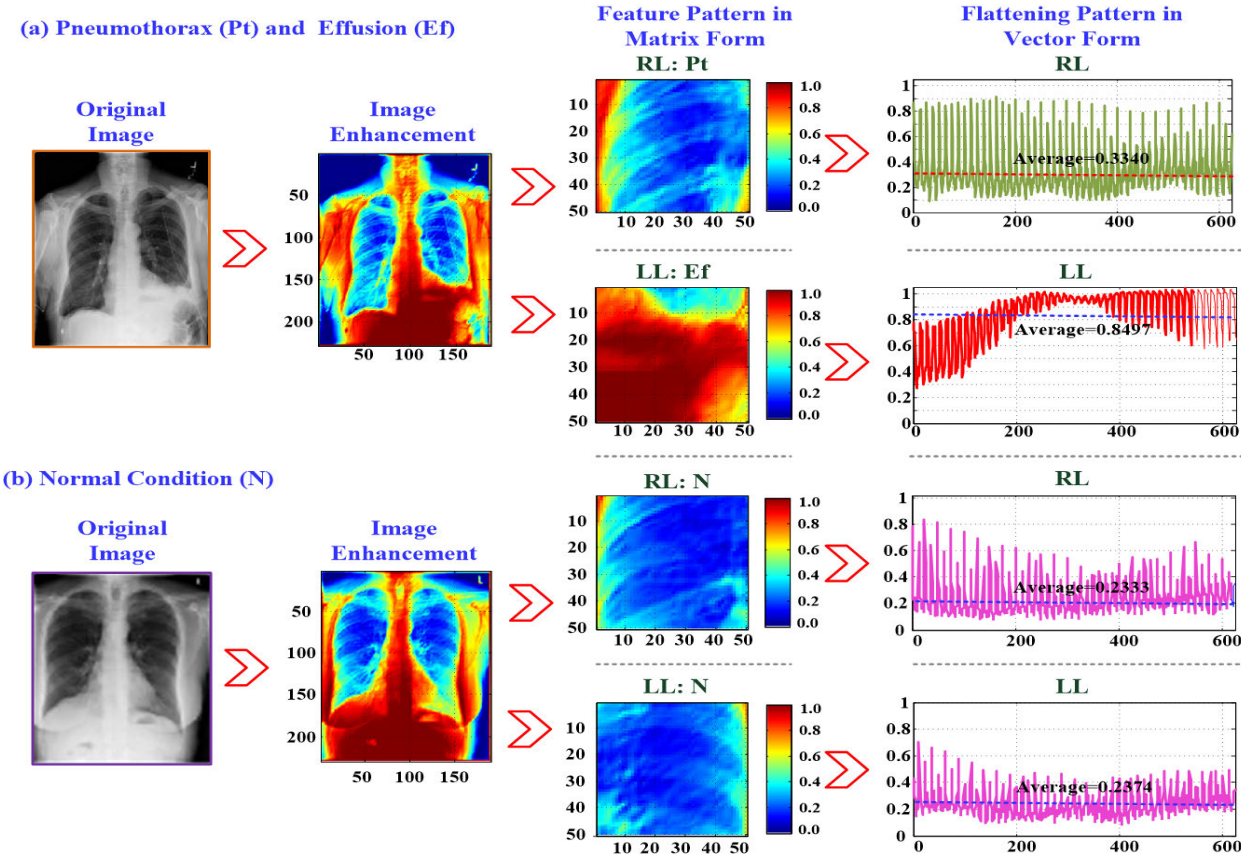
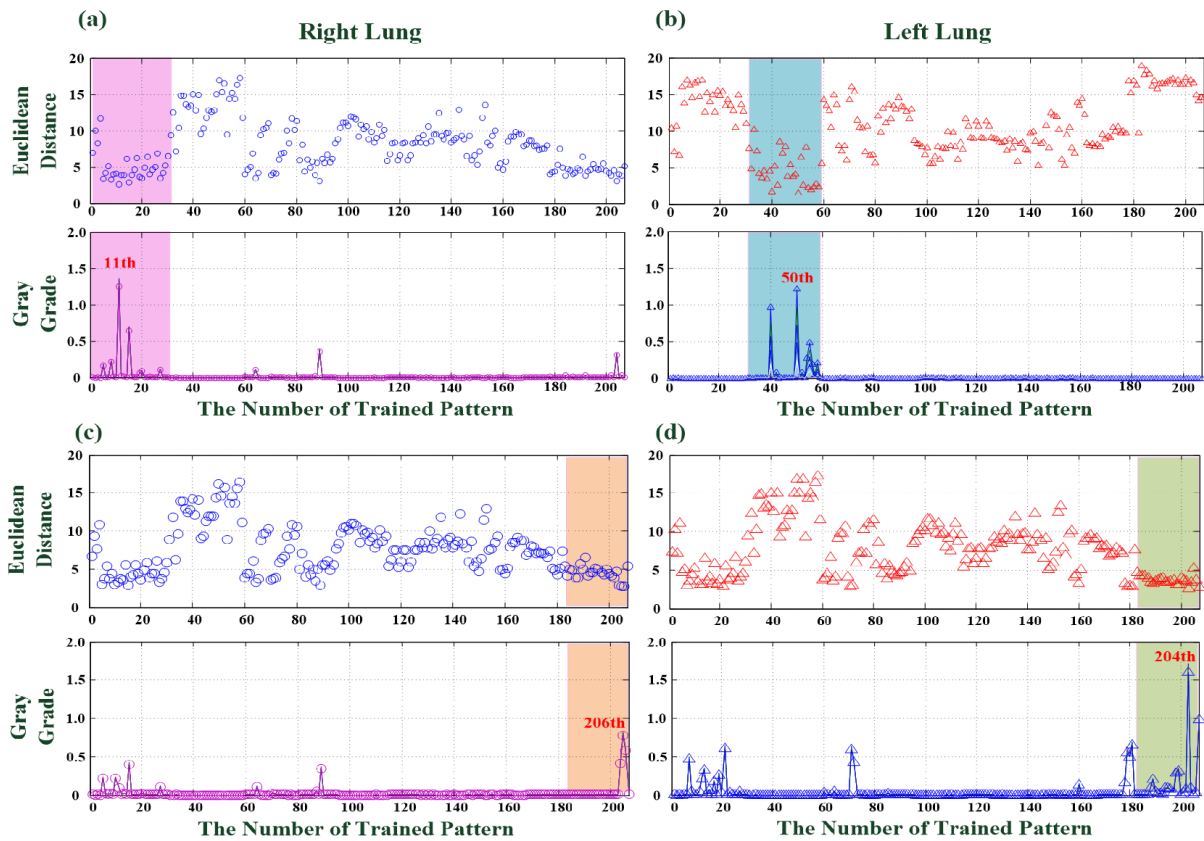


**FIGURE 8.** Numerical results of digital image enhancement, feature extraction, pooling and flattening processes. Case study of subjects (a) with Pt and Ef and (b) with a normal (N) condition.

two untrained patterns were similar to the #11th and #50th trained patterns within the subdatasets of Classes #Pt (pink color region) and #Ef (light-blue color region), as seen in

Figures 9(a) and 9(b). The GG functions with the parameter  $\xi$  indicated the “disease present” from the “disease absent” by using Equations (10) to (14) and confirmed that the GGS were



Note: (1) Pt: No. 1-34; (2) Ef: No. 35-59; (3) E: No. 60-74; (4) In: No. 75-102; (5) M: No. 103-127; (6) P: No. 128-157; (7) F: No. 158-182; (8) N: No. 183-207

**FIGURE 9. Euclidean distances (EDs) and gray grades (GGs) versus the number of trained patterns for numerical computation results.**  
**(a) and (b) Case studies on Pt and Ef; (c) and (d) case studies on N.**

between 0 and  $\xi$ . Through numerical analysis,  $\xi$  would only change the values of GG, but it would not change the gray relational grade ranking. Then, the final outputs of the two classes were computed using Equations (16) to (18):

- outputs in RL:  $Y = [0.7525, 0.0000, 0.0427, 0.1017, 0.0000, 0.0000, 0.0061, 0.1313]$  and  $O_1 = 1$  for identifying the Class #Pt in RL,
- outputs in LL:  $Y = [0.0000, 1.0000, 0.0000, 0.0000, 0.0000, 0.0000, 0.0000, 0.0000]$  and  $O_2 = 1$  for identifying the Class #Ef in LL.

The entire process took an average CPU time of 0.1610 s to identify the possible classes. The above case study showed that the proposed CADM tool could screen the pathology classes on multi-label classification and demonstrated a high confidence in this regard. In addition, the numerical results of digital image processes for a subject with the N condition are shown in Figure 8(b). Given the two untrained patterns (pink line patterns, mean gray gradients = 0.2333 and 0.2374, respectively, as seen in Figure 8(b)), the screening results indicated a higher similarity degree (#206th and #204th) in orange and olive regions, as seen in Figures 9(c) and 9(d), respectively. Then, the final outputs of RL and LL were computed as follows:

- outputs in RL:  $Y = [0.4235, 0.0000, 0.1026, 0.0190, 0.0000, 0.0000, 0.0117, 0.5295]$  and  $O_8 = 1$  for identifying the Class #N in RL,

- outputs in LL:  $Y = [0.0849, 0.0000, 0.0128, 0.0003, 0.0000, 0.0000, 0.0350, 0.8786]$  and  $O_8 = 1$  for identifying the Class #N in LL.

Both case studies showed the true positive (Pt and Ef) and true negative (N) for the possible identification of classes with a higher confidence. This finding confirmed that the proposed CADM tool could provide a scientific approach for the rapid screening of typical lung diseases.

## B. K-FOLD CROSS-VALIDATION WITH UNTRAINED PATTERNS

At the recalling stage, the untrained patterns were randomly selected from the remaining datasets: 34 Pts, 25 Efs, 15 Es, 28 Ins, 25 Ms, 30 Ps, 25 Fs, and 25 Ns (Table 2). Tenfold cross-validation was conducted to evaluate the performance of the GRA-based classifier with 2D FOC. Recall (%), precision (%), accuracy (%), and F1 score (F measurement) [41] were used as indices to validate the screening performance by using true positive (TP), false positive (FP), and false negative (FN). The experimental results of the GRA-based classifier are presented in Table 2. A mean recall of 98.68% and a mean precision of 82.42% for identifying the TP and a mean accuracy of 83.57% for determining the possible correct classes were obtained in tenfold cross-validation as mean mismatches (34) with 6 failures in Pt, 4 failures in Ef, 3 failures in E, 5 failures in In, 4 failures in M, 6 failures in P,

**TABLE 2.** Experimental results of 10-fold cross validation for GRA-based classifier with 2D FOC.

Cross Validation	Trained Patterns	Untrained Patterns	Recall (%)	Precision (%)	Accuracy (%)	F1 Score
1	Random Selection  34 Pts, 25 Efs, 15 Es, 28 Ins, 25 Ms, 30 Ps, 25 Fs, 25 Ns  Disease Present: 182 patterns  Disease Absent: 25 patterns  Total of Trained Pattern: 207	Random Selection  34 Pts, 25 Efs, 15 Es, 28 Ins, 25 Ms, 30 Ps, 25 Fs, 25 Ns  Disease Present: 182 patterns  Disease Absent: 25 patterns  Total of Trained Pattern: 207	98.73 (TP: 156, FN: 2)	85.31 (TP: 156, FP: 26)	86.47 (28 failures)	0.9176
2			98.65 (TP: 146, FN: 2)	80.22 (TP: 146, FP: 36)	81.64 (38 failures)	0.8848
3			98.69 (TP: 151, FN: 2)	82.97 (TP: 151, FP: 31)	84.06 (33 failures)	0.9015
4			98.67 (TP: 148, FN: 2)	81.32 (TP: 148, FP: 34)	82.61 (36 failures)	0.8916
5			98.68 (TP: 149, FN: 2)	81.87 (TP: 149, FP: 33)	83.09 (35 failures)	0.8949
6			98.66 (TP: 147, FN: 2)	80.77 (TP: 147, FP: 35)	82.12 (37 failures)	0.8882
7			98.70 (TP: 152, FN: 2)	83.52 (TP: 152, FP: 30)	84.54 (32 failures)	0.9048
8			98.68 (TP: 150, FN: 2)	82.42 (TP: 150, FP: 32)	83.57 (34 failures)	0.8982
9			98.72 (TP: 154, FN: 2)	84.62 (TP: 154, FP: 28)	85.51 (30 failures)	0.9112
10			98.66 (TP: 147, FN: 2)	80.77 (TP: 147, FP: 35)	82.13 (37 failures)	0.8882
Average (%)			98.68	82.42	83.57	0.8981

**TABLE 3.** Experimental results of 10-fold cross validation for traditional GRA-based classifier with 2D FOC.

Cross Validation	Trained Patterns	Untrained Patterns	Recall (%)	Precision (%)	Accuracy (%)	F1 Score
1	Random Selection  34 Pts, 25 Efs, 15 Es, 28 Ins, 25 Ms, 30 Ps, 25 Fs, 25 Ns  Disease Present: 182 patterns  Disease Absent: 25 patterns  Total of Trained Pattern: 207	Random Selection  34 Pts, 25 Efs, 15 Es, 28 Ins, 25 Ms, 30 Ps, 25 Fs, 25 Ns  Disease Present: 182 patterns  Disease Absent: 25 patterns  Total of Trained Pattern: 207	99.28 (TP: 138, FN: 1)	75.82 (TP: 138, FP: 44)	78.26 (45 failures)	0.8598
2			98.61 (TP: 142, FN: 2)	78.02 (TP: 142, FP: 40)	79.71 (42 failures)	0.8712
3			99.27 (TP: 136, FN: 1)	76.04 (TP: 136, FP: 46)	78.45 (47 failures)	0.8527
4			99.29 (TP: 140, FN: 1)	76.92 (TP: 140, FP: 42)	79.23 (43 failures)	0.8669
5			99.27 (TP: 136, FN: 1)	76.04 (TP: 136, FP: 46)	78.45 (47 failures)	0.8527
6			99.28 (TP: 138, FN: 1)	75.82 (TP: 138, FP: 44)	78.26 (45 failures)	0.8598
7			99.29 (TP: 140, FN: 1)	76.92 (TP: 140, FP: 42)	79.23 (43 failures)	0.8669
8			99.28 (TP: 138, FN: 1)	75.82 (TP: 138, FP: 44)	78.26 (45 failures)	0.8598
9			99.29 (TP: 140, FN: 1)	76.92 (TP: 140, FP: 42)	79.23 (43 failures)	0.8669
10			99.27 (TP: 136, FN: 1)	76.04 (TP: 136, FP: 46)	78.45 (47 failures)	0.8527
Average (%)			99.28	76.04	78.45	0.8619

Note: (1) Recall (%) =  $\frac{TP}{TP + FN} \times 100\%$ , where TP and FN are the true positive and false negative, respectively;

(2) Precision (%) =  $\frac{TP}{TP + FP} \times 100\%$ , where TP and FP are true positive and false positive, respectively;

(3) Accuracy (%) =  $\frac{TP + TN}{TP + FN + TN + FP} \times 100\%$ ;

(4) F1 Score =  $\frac{2TP}{2TP + FP + FN}$ ;

(5) The output of traditional GRA is defined as  $g(k) = \frac{\Delta d_{\min} + \xi \Delta d_{\max}}{ED(k) + \xi \Delta d_{\max}}$ ,  $k=1, 2, 3, \dots, 207$ ,  $\xi \in (0, 5]$ , where  $\Delta d_{\max}$  and  $\Delta d_{\min}$  are

computed using Equation (14);  $ED(k)$  is computed using Equations (11) and (12)..

4 failures in F, and 2 failures in N. A precision of 82.42% was also referred to as a positive predictive value (PPV), which was greater than 80.00%, to evaluate the performance of the automatic predictor. The recall (%) was defined as the sensitivity with a higher value to identify the possible class in the

studied lung diseases. The mean F1 score also showed a high value of 0.8981 to evaluate the performance of the proposed GRA-based classifier, which could provide promising results for rapid screening. The best F1 score was close or equal to 1.0000. The recalling stage required approximately 6.0580 s

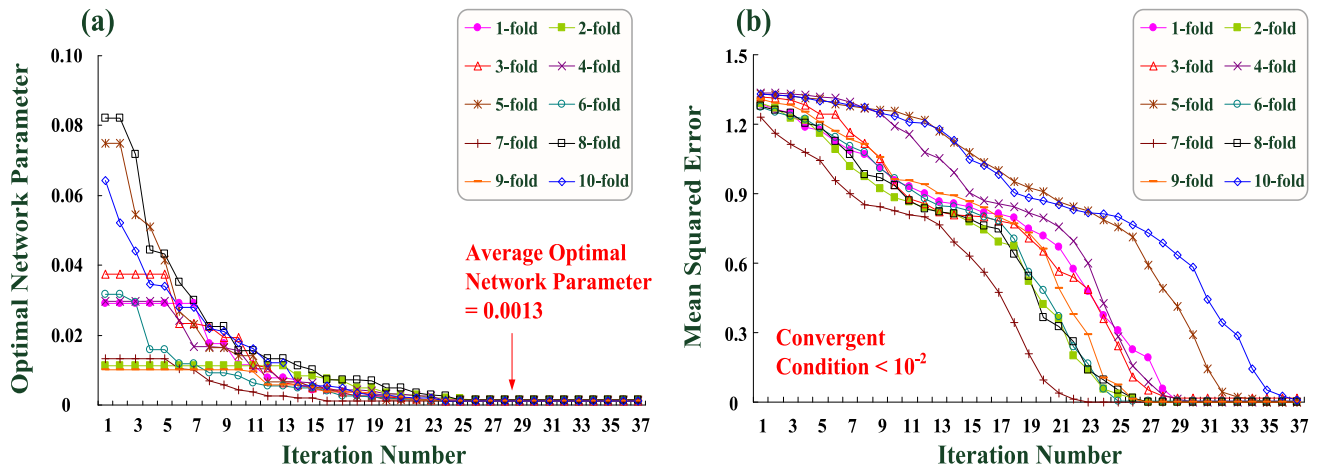


**FIGURE 10.** GRNN-based classifier training. (a) Optimal network parameters versus iteration computations by using the PSO algorithm. (b) Mean squared errors versus iteration computations.

of CPU execution time to complete each fold cross-validation without iteration computations.

### C. COMPARISON WITH A TRADITIONAL GRA-BASED CLASSIFIER AND MULTILAYER CONNECTING NETWORK

The 2D FOC, maximum pooling, flattening processes and a traditional GRA-based classifier or a multilayer connecting network can also be integrated into a machine vision classifier. In this study, a generalized regression neural network (GRNN) [26], [27] with an optimization algorithm was used to train the multilayer connecting network. For the same datasets, 207 paired input-output trained patterns were randomly selected from the datasets at each training stage to train the traditional GRA-based and GRNN-based classifiers. In each fold cross-validation, the remaining datasets as untrained patterns were used to validate the classifier. In the traditional GRA-based classifier,  $RC$  was also set to  $\xi = 5$  in each GG function (as seen in Note (5) in Table 3). With tenfold cross-validation, as seen in Table 3, a mean recall of 99.28%, a mean precision of 76.04%, a mean accuracy of 78.45% and a mean F1 score of 0.8619 were obtained as mean mismatches (43) with 5 failures in Pt, 3 failures in Ef, 8 failures in E, 11 failures in In, 5 failures in M, 5 failures in P, 5 failures in F and 1 failure in N. Precision was less than 80.00% for identifying the possible “disease present.” Its F1 score was also less than that of the proposed GRA-based classifier.

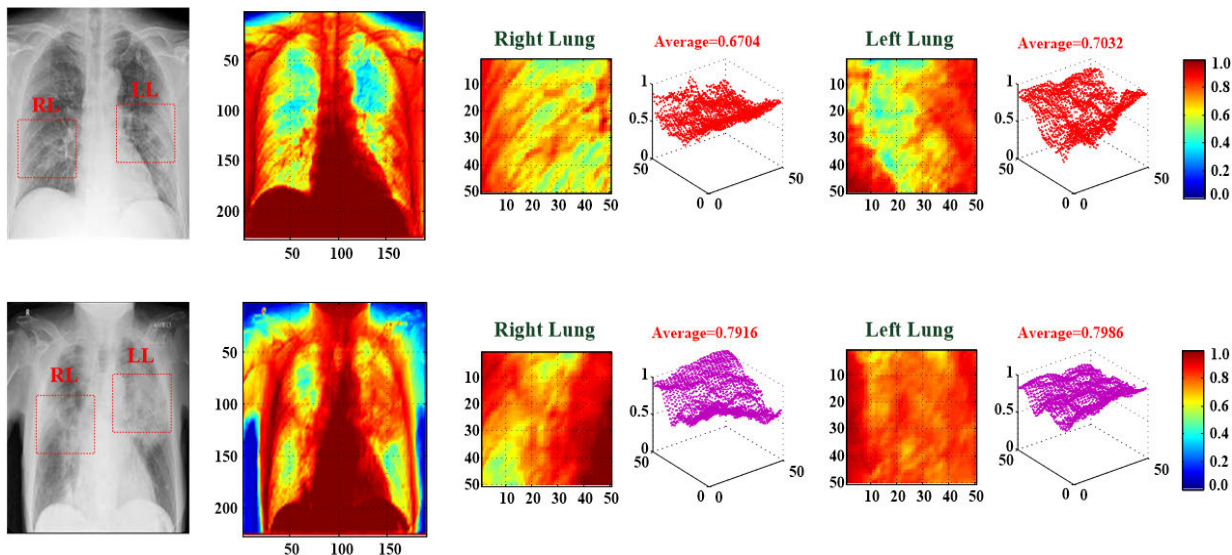
In the GRNN-based multilayer connecting network, a classifier consisting of 625 input nodes, 207 pattern nodes, 9 summation node, and 8 output nodes was constructed. At the training stage, particle swarm optimization [26], [27] was used to search the optimal network parameters of the Gaussian functions in an RBN with a particle population size of 30, a maximum iteration number of 50, and a convergent condition of  $\leq 10^{-2}$ . The iteration operations required  $< 40$  iterative computations (mean CPU execution time of

$< 6.2524$  s) to reach the pre-specific convergent condition in 10 training stages. The mean optimal network parameter of 0.0013 could be obtained to minimize the mean squared error. This observation is presented in the plots of optimal network parameters and mean squared errors versus the iteration computations for the training of the GRNN-based classifier in Figures 10 (a) and 10(b). At the recalling stage, for the randomly selected untrained datasets with 10-fold cross-validation, a mean recall of 97.35%, a mean precision of 80.71%, a mean accuracy of 81.11%, and a mean F1 score of 0.8825 were obtained (Table 4) as mean mismatches (37) with 7 failures in Pt, 2 failures in Ef, 4 failures in E, 5 failures in In, 5 failures in M, 4 failures in P, 6 failures in F, and 4 failures in N. The F1 score had a promising value greater than 80.00% for identifying the TP cases. The recall (%), precision (%), accuracy (%), and F1 score of the proposed GRA-based classifier were higher than those of the GRNN-based classifier to be used as clinical indications for the rapid screening of typical lung diseases. In addition, the GRNN-based classifier had some limitations, including (1) the need for iteration computations to adjust the optimal network parameter; (2) the need for an optimization algorithm to search for optimal network parameters; and (3) the need for assigned initial conditions, such as initial network parameter, particle population size, acceleration parameters, and convergent condition.

In addition, for a multi-label classification problem, feature attention network (FAN), fully/sparse fully convolutional network (FCN/SFCN), and deep convolutional neural network (DCNN) have also been applied to recognize the multi objects or attributes in an image, such as face labeling, video classification, and activity detection [1], [44], [45]. A FAN consisted of feature refinement network and correlation learning network [44] which could extract the multi-scale features and context information for recognizing the obvious objects in spatial features and the disappearing objects in

**TABLE 4.** Experimental results of 10-fold cross validation for multilayer connecting network with 2D FOC.

Cross Validation	Trained Patterns	Untrained Patterns	Recall (%)	Precision (%)	Accuracy (%)	F1 Score
1	Random Selection 34 Pts, 25 Efs, 15 Es, 28 Ins, 25 Ms, 30 Ps, 25 Fs, 25 Ns Disease Present: 182 patterns Disease Absent: 25 patterns Total of Trained Pattern: 207	Random Selection 34 Pts, 25 Efs, 15 Es, 28 Ins, 25 Ms, 30 Ps, 25 Fs, 25 Ns Disease Present: 182 patterns Disease Absent: 25 patterns Total of Trained Pattern: 207	97.33 (TP: 146, FN: 4)	80.22 (TP: 146, FP: 36)	80.68 (40 failures)	0.8795
2			97.40 (TP: 150, FN: 4)	82.42 (TP: 150, FP: 32)	82.61 (36 failures)	0.8928
3			97.35 (TP: 147, FN: 4)	80.77 (TP: 147, FP: 35)	81.16 (39 failures)	0.8829
4			97.32 (TP: 145, FN: 4)	79.67 (TP: 145, FP: 37)	80.19 (41 failures)	0.8761
5			97.37 (TP: 148, FN: 4)	81.32 (TP: 148, FP: 34)	81.64 (38 failures)	0.8862
6			97.30 (TP: 144, FN: 4)	79.12 (TP: 144, FP: 38)	79.71 (42 failures)	0.8727
7			97.39 (TP: 149, FN: 4)	81.87 (TP: 149, FP: 33)	82.13 (37 failures)	0.8896
8			97.40 (TP: 150, FN: 4)	82.42 (TP: 150, FP: 32)	82.61 (36 failures)	0.8928
9			97.26 (TP: 142, FN: 4)	78.02 (TP: 142, FP: 40)	78.74 (44 failures)	0.8659
10			97.37 (TP: 148, FN: 4)	81.32 (TP: 148, FP: 34)	81.64 (38 failures)	0.8862
Average (%)			97.35	80.71	81.11	0.8825

**FIGURE 11.** Case studies on chest X-ray images of a subject with pneumonia related to COVID-19. (a) Subject had patchy ground-glass opacities in the right upper and lower lobes of the lung and patchy consolidation in the left middle lobe to the left lower lobe of the lung [42]. (b) Subject had pneumonia related to COVID-19 with hypertension and type 2 diabetes mellitus [43].

semantic features. However, not all features were informative, which were required to distinguish the key features using image enhancement process. FCN/SFCN had good capability in feature extraction and learning representation for semantic segmentation and multi-label classification [45]. Its network was too complicated with multi-convolutional layers and pooling layers, thus, a large network size and huge parameters would limit the adaptive capacity to retrain the FCN/SFCN with new training patterns in real-world application. In literature [1], DCNN also consisted of convolutional layers, pooling layers, and a fully connecting network, which was carried out a classifier for P localization from chest X-ray images. However, DCNN method also required assigning the

multiple convolutional layers and pooling layers for feature extraction and multiple hidden layers to fully connected network weights. Hence, determining the convolutional mask sizes, the convolutional mask parameters, structure of the multilayer network (including hidden layers, hidden nodes, and connected network parameters), and the large amount of training patterns are also major concerns. Therefore, the above presented methods provided promising results in classification tasks, however, too many multi-connected structure would increase the rate of the design cycle and computational time.

The comparisons presented in Tables 2 to 4 revealed that the proposed multilayer machine vision classifier provided

promising results and clinical indications in PPV. The proposed GRA-based method involved a straightforward mathematical operation to process numerical computations without optimization algorithms and iteration computations but with self-tuning of the standard deviation of the GG function by determining the maximum and minimum differences between an untrained pattern and trained patterns. This method was an adaptive pattern mechanism to continually add real-world datasets without parameter adjustment and assignment. For example, it could be applied to examine the chest X-ray images of a patient with pneumonia related to novel coronavirus disease (COVID)- 19 [42], [43] (as seen in Figure 11). Only RC was required to be assigned in clinical applications, and the experienced value of  $\xi \gg 1$  was selected to make the difference more distinguishable and identify the possible class. Gaussian- based GG functions in an RBN could transform the feature patterns to a nonlinearity and a high-dimensional space to solve nonlinear separable classification problems. Given the feature patterns (mean gray gradient = 0.6868 and 0.7951, respectively, as seen in Figure 11), the GRA-based classifier could also be used to accurately identify “*Class P* (mean output,  $y_6 > 0.8000$ )” with an advanced lung disease. The outcomes of the proposed classifier model were better than those of a traditional GRA-based classifier and a GRNN-based classifier.

#### IV. CONCLUSION

In this study, a multilayer machine vision classifier was developed to rapidly screen any lesion in the right and left lung zones. This classifier consisted of a 2D FOC operation, a maximum pooling process, a flattening process and a GRA-based classifier. For all case studies, the 2D FOC operation with the fractional-order parameter  $v = 0.3$  was used to enhance the low-contrast chest X-ray images and to make the lesion more visible for further feature extraction and pattern recognition. With a specific B-box ( $50 \times 50$  pixels) within the ROI, the screenshot process was used to select the testing feature patterns, which were fed into the machine vision classifier and displayed on a computer screen. After digital image processes were completed, the GRA-based classifier was employed to identify the possible class in the bilateral lungs. The feasibility of the proposed multilayer fractional-order machine vision classifier was validated through 10-fold cross-validation. For the rapid screening of typical lung diseases, this classifier had a mean recall of 98.68%, a mean precision of 82.42%, a mean accuracy of 83.57% and a mean F1 score of 0.8981, with a mean of 33 mismatches in TP and TN cases. The F1 score of the GRA-based classifier was higher than that of traditional a GRA-based classifier and a multilayer connecting network for TP case identification. Hence, the proposed multilayer classifier provided an automatic CADM tool to separate “*disease present*” from “*disease absent*” and enabled clinicians to focus on clinical treatments.

For clinical applications, a computer vision and automatic inspection tool was used to assist clinicians/radiologists in

disease diagnosis and rapid medical image screening. In real situations or COTS platforms, new chest X-ray images could be continually mined if some suggestions were provided by clinicians/radiologists, or new cases were produced in clinical investigations; examples of these cases with chest radiography scans included subjects with COVID-19, severe acute respiratory syndrome (SARS), aspiration pneumonia (AP), or acute respiratory distress syndrome (ARDS). An X-ray image of a patient with COVID-19 is shown in Figure 11 [42], [43]. The X-ray image findings of the lungs of a patient with COVID-19-related pneumonia were analyzed, and feature patterns, such as patchy ground-class opacities, pure/mixed ground-glass opacities, patchy consolidation, or large confluent lesions, were collected as comparative sequences for updating the trained patterns in the feature matrix  $\Phi$  as shown in Equation (15). After high-quality X-ray images with annotations were obtained, datasets could be continuously added to the current database with advanced /novel lung diseases. The proposed GRA method could adapt itself in a new pattern mechanism by adding trained patterns without statistical methods, complex iteration computations, and parameter assignments. Therefore, its pattern mechanism was easily adapted in real-world applications and keep the intended medical purpose during diagnosis. The proposed method could be used as a CADM tool or an SaMD. It could also be integrated in medical devices as a SiMD.

#### ABBREVIATIONS

---

Pt	Pneumothorax
Ef	Pleural Effusion
E	Emphysema
In	Inflammation
M	Mass
P	Pneumonia
F	Fibrosis
COPD	Chronic Obstructive Pulmonary Disease
NIH	Nation Institutes of Health
ROI	Region of Interest
B-box	Bounding Box
RL	Right Lung
LL	Left Lung
G-L	Grümwald-Letnikov
R-L	Riemann-Liouville
FOC	Fractional-Order Convolution
RBN	Radial Bayesian Network
GRA	Gray Relational Analysis
GG	Gray Grade
ED	Euclidean Distance
RC	Recognition Coefficient
GUI	Graphic User Interface
CADM	Computer-Aided Decision-Making
COTS	Commercial off-the-Shelf
PPV	Positive Predictive Value
FAT	Feature Attention Network
FCN/SFCN	Fully / Sparse Fully Convolutional Network
DCNN	Deep Convolutional Neural Network
SaMD	Software as a Medical Device
SiMD	Software in a Medical Device
COVID	Novel Coronavirus Disease

---

## LIST OF FORMULAS SYMBOLS AND NOMENCLATURES

$\frac{d^v I(x, y)}{dx^v}, \frac{d^v I(x, y)}{dy^v}$	Fractional-Order Differentiator
$v$	Fractional-Order Parameter
$\Gamma(\bullet)$	Gamma Function
$I(x, y)$	Pixel Value at Location $(x, y)$ in an Image
$\nabla^v I(x, y)$	Fractional-Order Gradient
$\nabla I$	Normalize the Fractional-Order Gradient
$G_x^v I(x, y)$	Convolution Process at Horizontal Direction
$G_y^v I(x, y)$	Convolution Process at Vertical Direction
$M_x, M_y$	Fractional-Order Mask
$\Phi_0$	Reference Sequence (Testing Pattern)
$\Phi_k$	Comparative Sequences (Training Pattern)
$g(k)$	Gray Grade (GG)
$ED(k)$	Euclidean Distance
$\Delta d_{(k)}$	Differences between a Testing Pattern and Training Pattern
$\Delta d_{max}, \Delta d_{min}$	Maximum and Minimum Differences
$\sigma^2$	Variance
$\xi$	Recognition Coefficient
$w_{kj}$	Weighting Value
$Y$	Output Vector
$O$	Final Output Vector

## REFERENCES

- [1] I. Sirazdinov, M. Kholiavchenko, T. Mustafaev, Y. Yixuan, R. Kuleev, and B. Ibragimov, “Deep neural network ensemble for pneumonia localization from a large-scale chest X-Ray database,” *Comput. Electr. Eng.*, vol. 78, pp. 388–399, Sep. 2019.
- [2] (2020). *National Institute of Environmental Health Sciences (NIH), Lung Diseases*. [Online]. Available: <https://niehs.nih.gov/health/topics/Conditions/lung-disease/index.cfm#footnote1>.
- [3] J. Marx, *Rosen’s Emergency Medicine: Concepts and Clinical Practice*, 7th ed. Philadelphia, PA, USA: Mosby/Elsevier, 2010, pp. 393–396.
- [4] B. S. Kancharla, M. K. Dishop, S. S. Rothenberg, and L. L. Fan, “Diffuse pulmonary infiltrates in an immunocompromised patient,” *J. Allergy Clin. Immunology*, vol. 121, no. 2, pp. 540–542, Feb. 2008.
- [5] C.-F. Weng, L.-J. Chen, C.-W. Lin, H.-M. Chen, H. H.-C. Lee, T.-Y. Ling, and F.-Y. Hsiao, “Association between the risk of lung cancer and influenza: A population-based nested case-control study,” *Int. J. Infectious Diseases*, vol. 88, pp. 8–13, Nov. 2019.
- [6] T.-Y.-D. Cheng, S. M. Cramb, P. D. Baade, D. R. Youlden, C. Nwogu, and M. E. Reid, “The international epidemiology of lung cancer: Latest trends, disparities, and tumor characteristics,” *J. Thoracic Oncol.*, vol. 11, no. 10, pp. 1653–1671, Oct. 2016.
- [7] D. Planchard and B. Besse, “Lung cancer in never—Smokers,” *Eur. Respiratory J.*, vol. 45, no. 5, pp. 1214–1217, 2015.
- [8] H. Yu, “Management of pleural effusion, empyema, and lung abscess,” *Seminars Interventional Radiol.*, vol. 28, no. 1, pp. 75–86, 2011.
- [9] L. Vetrugno, G. M. Guadagnin, D. Orso, E. Boero, E. Bignami, and T. Bove, “An easier and safe affair, pleural drainage with ultrasound in critical patient: A technical note,” *Crit. Ultrasound J.*, vol. 10, no. 1, pp. 1–10, Dec. 2018.
- [10] P.-Y. Chen, C.-H. Lin, C.-D. Kan, N.-S. Pai, W.-L. Chen, and C.-H. Li, “Smart pleural effusion drainage monitoring system establishment for rapid effusion volume estimation and safety confirmation,” *IEEE Access*, vol. 7, pp. 135192–135203, 2019.
- [11] K. Sebulkingam. *Essential of Medical Physiology*, 5th ed. New Delhi, India: Jaypee Brothers, 2003.
- [12] E. Usta, M. Mustafi, and G. Ziemer, “Ultrasound estimation of volume of postoperative pleural effusion in cardiac surgery patients,” *Interact. CardioVascular Thoracic Surg.*, vol. 10, no. 2, pp. 204–207, Feb. 2010.
- [13] M. P. Moy, J. M. Levsky, N. S. Berko, A. Godelman, V. R. Jain, and L. B. Haramati, “A new, simple method for estimating pleural effusion size on CT scans,” *Chest*, vol. 143, no. 4, pp. 1054–1059, Apr. 2013.
- [14] H. M. Zaeim, C. Scheffer, M. Blanckenberg, and K. Dellimore, “Evaluation of the use of frequency response in the diagnosis of pleural effusion on a phantom model of the human lungs,” in *Proc. 36th Annu. Int. Conf. IEEE Eng. Med. Biol. Soc.*, Aug. 2014, pp. 3418–3421.
- [15] S. A. Rezaieh and A. M. Abbosh, “Review of systems for the detection and monitoring of accumulated fluids in the human torso,” in *Proc. Int. Symp. Antennas Propag.*, Nov. 2015, pp. 1–4.
- [16] Z. Li, X. Li, Z. Zhu, S. Zeng, Y. Wang, Y. Wang, and A. Li, “Signal analysis of electrocardiogram and statistical evaluation of myocardial enzyme in the diagnosis and treatment of patients with pneumonia,” *IEEE Access*, vol. 7, pp. 113751–113759, 2019.
- [17] F. Andreotti, F. Grasser, H. Malberg, and S. Zaunseider, “Non-invasive fetal ECG signal quality assessment for multichannel heart rate estimation,” *IEEE Trans. Biomed. Eng.*, vol. 64, no. 12, pp. 2793–2802, Dec. 2017.
- [18] Y.-F. Pu, J.-L. Zhou, and X. Yuan, “Fractional differential mask: A fractional differential-based approach for multiscale texture enhancement,” *IEEE Trans. Image Process.*, vol. 19, no. 2, pp. 491–511, Feb. 2010.
- [19] Y. Zhang, Y.-F. Pu, and J.-L. Zhou, “Construction of fractional differential masks based on Riemann-Liouville definition,” *J. Comput. Inf. Syst.*, vol. 6, no. 10, pp. 3191–3199, 2010.
- [20] C.-H. Lin, C.-D. Kan, W.-L. Chen, and P.-T. Huang, “Application of two-dimensional fractional-order convolution and bounding box pixel analysis for rapid screening of pleural effusion,” *J. X-Ray Sci. Technol.*, vol. 27, no. 3, pp. 517–535, Jul. 2019.
- [21] T. Lindeberg, E. Detection, and M. Hazewinkel, Ed., *Encyclopedia of Mathematics*. Norwell, MA, USA: Kluwer, 2001.
- [22] Q. Yang, D. Chen, T. Zhao, and Y. Chen, “Fractional calculus in image processing: A review,” *Fractional Calculus Appl. Anal.*, vol. 19, no. 5, pp. 1–26, Jan. 2016.
- [23] B. T. Krishna, “Studies on fractional order differentiators and integrators: A survey,” *Signal Process.*, vol. 91, no. 3, pp. 386–426, 2011.
- [24] H. Chougrad, H. Zouaki, and O. Alheyane, “Deep convolutional neural networks for breast cancer screening,” *Comput. Methods Programs Biomed.*, vol. 157, pp. 19–30, Apr. 2018.
- [25] S. Wan, Y. Liang, Y. Zhang, and M. Guizani, “Deep multi-layer perceptron classifier for behavior analysis to estimate Parkinson’s disease severity using smartphones,” *IEEE Access*, vol. 6, pp. 36825–36833, 2018.
- [26] C.-D. Kan, W.-L. Chen, C.-H. Lin, J.-N. Wang, P.-J. Lu, M.-Y. Chan, and J.-T. Wu, “Customized handmade pulmonary valved conduit reconstruction for children and adult patients using meta-learning based intelligent model,” *IEEE Access*, vol. 6, pp. 21381–21396, 2018.
- [27] T.-L. Yang, C.-H. Lin, W.-L. Chen, H.-Y. Lin, C.-S. Su, and C.-K. Liang, “Hash transformation and machine learning-based decision-making classifier improved the accuracy rate of automated Parkinson’s disease screening,” *IEEE Trans. Neural Syst. Rehabil. Eng.*, vol. 28, no. 1, pp. 72–82, Jan. 2020.
- [28] C.-H. Lin, “Assessment of bilateral photoplethysmography for lower limb peripheral vascular occlusive disease using color relation analysis classifier,” *Comput. Methods Programs Biomed.*, vol. 103, no. 3, pp. 121–131, Sep. 2011.
- [29] Y. Cenglin, “Application of gray relational analysis method in comprehensive evaluation on the customer satisfaction of automobile 4S enterprises,” *Phys. Procedia*, vol. 33, pp. 1184–1189, Jan. 2012.
- [30] K. S. Prakash, P. M. Gopal, and S. Karthik, “Multi-objective optimization using taguchi based grey relational analysis in turning of rock dust reinforced aluminum MMC,” *Measurement*, vol. 157, Feb. 2020, Art. no. 107664.
- [31] Y. Wu, F. Zhou, and J. Kong, “Innovative design approach for product design based on TRIZ, AD, fuzzy and Grey relational analysis,” *Comput. Ind. Eng.*, vol. 140, Jan. 2020, Art. no. 106276.
- [32] F. Sarrafa and S. H. Nejad, “Improving performance evaluation based on balanced scorecard with grey relational analysis and data envelopment analysis approaches: Case study in water and wastewater companies,” *Eval. Program Planning*, vol. 79, pp. 1–12, Apr. 2020.
- [33] Nation Institutes of Health (NIH). (2019). *Clinical Center, Images are Available Via Box*. [Online]. Available: <https://nihcc.app.box.com/v/ChestXray-NIHCC>
- [34] X. Wang, Y. Peng, L. Lu, Z. Lu, M. Bagheri, and R. M. Summers, “ChestX-ray8: Hospital-scale chest X-Ray database and benchmarks on weakly-supervised classification and localization of common thorax diseases,” in *Proc. IEEE Conf. Comput. Vis. Pattern Recognit. (CVPR)*, Jul. 2017, pp. 2097–2106.
- [35] Nation Institutes of Health. (2017). *NIH Clinical Center Provides One of the Largest Publicly Available Chest X-Ray Datasets to Scientific Community*. [Online]. Available: <https://www.nih.gov/news-events/news-releases/nih-clinical-center-provides-one-largest-publicly-available-chest-x-ray-datasets-scientific-community>

- [36] Digital Health. (Nov. 2019). *U. S. FOOD & DRUG*. [Online]. Available: <https://www.fda.gov/medical-devices/digital-health>
- [37] Software as a Medical Device (SaMD). (Aug. 2018). *U. S. FOOD & DRUG*. [Online]. Available: <https://www.fda.gov/medical-devices/digital-health/software-medical-device-samd>
- [38] D. Chen, Y. Chen, and D. Xue, “1-D and 2-D digital fractional—Order savitzky-golay differentiator,” *Signal, Image Video Process.*, vol. 6, no. 3, pp. 503–511, 2012.
- [39] B. Li and W. Xie, “Adaptive fractional differential approach and its application to medical image enhancement,” *Comput. Electr. Eng.*, vol. 45, pp. 324–335, Jul. 2015.
- [40] C.-H. Lin, “Frequency-domain features for ECG beat discrimination using grey relational analysis-based classifier,” *Comput. Math. Appl.*, vol. 55, no. 4, pp. 680–690, Feb. 2008.
- [41] D. Chicco and G. Jurman, “The advantages of the Matthews correlation coefficient (MCC) over F1 score and accuracy in binary classification evaluation,” *BMC Genomics*, vol. 21, no. 1, pp. 1–13, Dec. 2020.
- [42] S. H. Yoon, K. H. Lee, J. Y. Kim, Y. K. Lee, H. Ko, K. H. Kim, C. M. Park, and Y.-H. Kim, “Chest radiographic and CT findings of the 2019 novel coronavirus disease (COVID-19): Analysis of nine patients treated in Korea,” *Korean J. Radiol.*, vol. 21, no. 4, pp. 1–7, 2020.
- [43] Sunny Jutla. (2020). *Adults Sim Scenario: COVID-19*. [Online]. Available: <https://em3.org.uk/foamed/6/3/2020/adults-sim-scenario-covid-19>
- [44] Z. Yan, W. Liu, S. Wen, and Y. Yang, “Multi-label image classification by feature attention network,” *IEEE Access*, vol. 7, pp. 98005–98013, 2019.
- [45] M. Dong, S. Wen, Z. Zeng, Z. Yan, and T. Huang, “Sparse fully convolutional network for face labeling,” *Neurocomputing*, vol. 331, pp. 465–472, Feb. 2019.



**CHIEN-MING LI** was born in 1959. He received the B.S. degree in science from National Taiwan University, Taipei, Taiwan, in 1982, and the M.D. and Ph.D. degrees in biomedical engineering from National Cheng Kung University, Tainan, Taiwan, in 1990 and 2014, respectively.

He is currently an Infectious Disease Specialist at the Chi Mei Medical Center, and an Associate Professor at the Medical College of National Cheng Kung University, Tainan. His research interests include medical applications of pattern recognition and MATLAB, computer-assisted diagnosis, and treatment of infectious disease.



**YING-CHE KUO** (Member, IEEE) received the B.S. and M.S. degrees in automatic control engineering from Feng Chia University, Taichung City, Taiwan, in 1986 and 1988, respectively, and the Ph.D. degree from the Institute of Communications Engineering, National Chiao Tung University, Hsinchu, Taiwan, in 2005.

In 1990, he joined the National Chin-Yi University of Technology, Taichung City, where he is currently a Professor with the Department of Electrical Engineering. His current research interests include intelligent vehicle, image processing and analysis, and application of embedded systems.



**NENG-SHENG PAI** received the B.S. and M.S. degrees from the Department of Automatic Control Engineering, Feng Chia University, Taichung City, Taiwan, in 1983 and 1986, respectively, and the Ph.D. degree from the Department of Electrical Engineering, National Cheng Kung University, Tainan, Taiwan, in December 2002.

He is currently a Professor at the Department of Electrical Engineering, National Chin-Yi University of Technology, Taichung City. He was the Chairman of the Department, from 2004 to 2007, and was also the Chairman of the Computer Center, National Chin-Yi University of Technology, from 2013 to 2017. His current research interests include fuzzy systems, artificial intelligence, imagine processing, advanced control systems, and microprocessor systems.



**CHIA-HUNG LIN** was born in Kaohsiung, Taiwan, in 1974. He received the B.S. degree in electrical engineering from the Tatung Institute of Technology, Taipei, Taiwan, in 1998, and the M.S. and Ph.D. degrees in electrical engineering from National Sun Yat-sen University, Kaohsiung, Taiwan, in 2000 and 2004, respectively.

He was a Professor at the Department of Electrical Engineering, Kao-Yuan University, Kaohsiung, from 2004 to 2017. Since 2018, he has been with the National Chin-Yi University of Technology, Taichung City, Taiwan, where he is currently a Professor at the Department of Electrical Engineering and a Researcher at the Artificial Intelligence Application Research Center. His research interests include neural network computing and its applications in power system and biomedical engineering, biomedical signal and image processing, healthcare, hemo-dynamic analysis, and pattern recognition.



**JIAN-XING WU** (Member, IEEE) was born in 1985. He received the B.S. and M.S. degrees in electrical engineering from the Southern Taiwan University of Science and Technology, Tainan, Taiwan, in 2007 and 2009, respectively, and the Ph.D. degree in biomedical engineering from National Cheng Kung University, Tainan, in 2014.

He was a Postdoctoral Research Fellow at the X-ray and IR Imaging Group, National Synchrotron Radiation Research Center, Hsinchu, Taiwan, from 2014 to 2017. He was also a Postdoctoral Research Fellow at the Department of Niche Biomedical LLC, California NanoSystems Institute, UCLA, Los Angeles, USA, from 2017 to 2018. Since 2019, he has been with the Department of Electrical Engineering, National Chin-Yi University of Technology, Taichung City, Taiwan, where is currently an Assistant Professor. His research interests include artificial intelligence applications in electrical engineering and biomedical engineering, biomedical signal processing and medical image processing, medical ultrasound, medical device design, and X-ray microscopy.



**PI-YUN CHEN** received the Ph.D. degree from the Graduate School of Engineering Science and Technology, National Yunlin University of Science and Technology, Douliu, Taiwan, in 2011.

She has been with the National Chin-Yi University of Technology, since 2019. She is currently an Associate Professor with the Department of Electrical Engineering, National Chin-Yi University of Technology, Taichung City, Taiwan, where she is also the Chief of the Department of Electrical Engineering. Her current research interests include neural network computing and its applications, digital signal and image processing, fuzzy systems, and advanced control systems.